





# Insight into the partial replacement of cement by ferronickel slags from New Caledonia

Manal Bouasria<sup>a</sup>, Laidi Babouri<sup>b</sup>, Fouzia Khadraoui<sup>a</sup>, Daniel Chateigner<sup>c</sup> , Stéphanie Gascoin<sup>c</sup>, Valérie Pralong<sup>c</sup>, Mohammed-Hichem Benzaama<sup>a</sup>, Beate Orberger<sup>d</sup> and Yassine El Mendili<sup>a</sup> 

<sup>a</sup>COMUE Normandie Université – Laboratoire ESITC, Epron, France; <sup>b</sup>École Normale Supérieure d'Enseignement Technologique de Skikda, Skikda, Algeria; <sup>c</sup>CRISMAT-ENSICAEN, UMR CNRS 6508, Université de Caen Normandie, Normandie Université, Caen, France; <sup>d</sup>GEOPS, Université Paris-Sud, UMR 8148 (CNRS-UPS), Orsay, France

## ABSTRACT

We investigate the mechanical characterisation of mortars incorporating ferronickel slags (FNS) as partial substitution for cement. The studied slags come from the ferronickel production in New Caledonia. The microstructural characterisation shows that these slags are polycrystalline heterogeneous material mainly composed of forsterite, quartz and enstatite in addition to silica glass. Cement is replaced by up to 20 wt.% of ferronickel slags in the mortars. This upper level of substitution is achieved without compromising mortar's strengths. For all mixes, the maximum compressive and flexural strengths at all curing ages is obtained with a 5 wt.% replacement of cement by ferronickel slags. The larger effectiveness of FNS is attributed to its larger silica content, which increases the polymerisation degree of the silica chains in the calcium silicate hydrate (C-S-H) structure. Slag recycling reduces the storage time, waste management and environmental impact. It significantly lowers costs related to metallurgical processing. Slag substitution for cement, also lowers the carbon footprint.

## ARTICLE HISTORY

Received 6 May 2020  
Accepted 19 August 2020

## KEYWORDS

Ferronickel slag; mineralogy; Raman; cement; mortar; C-S-H; carbon footprint

## 1. Introduction

The French company Société Le Nickel (SLN) produces nickel since 145 years in New Caledonia (Ashok et al., 2004; Ibrahim et al., 2018). The ferronickel slags (FNS) are manufacturing wastes, which currently amount to around 2 million tons per year. At present, only 8% of the annual production is used in cement production and road construction (Nickel, 2017). A stockpile of 25 million tons of FNS is immediately available (Nickel, 2017) for recycling. As it may present environmental risks for surface and groundwater, waste reduction and/or elimination should be performed.

The FNS from SLN is chemically stable and free of harmful substances (Nickel, 2017). It provides excellent properties such as high density, hardness and toughness, good compaction with high water permeability and high fire resistance with low thermal expansion (Nickel, 2017). It is widely used as asphalt aggregate, construction materials, moulding sand and as fertilisers. FNS presents an excellent potential for construction applications in the Pacific region and particularly for Australia, taking advantage of its strategic positioning and the increasing risk of the decreasing supply of natural aggregates and other supplementary cementitious materials. This product is largely employed in road construction, waterway stabilisation, agriculture and in many other sectors (Nickel, 2017). Further industrial application of these

alternative materials would contribute to minimise the extractive quarrying of primary aggregates thereby protecting more of natural resources and landscape.

The cement and concrete industries contribute considerably to CO<sub>2</sub> emissions (The European Cement Association [CEMBUREAU], 2017). Cement is one of the world's most widely used construction materials with about 4.6 billion tons of cement per year, releasing 4 billion tons of CO<sub>2</sub> and about 7% of the total anthropogenic carbon footprint (CEMBUREAU, 2017). The enhanced use of slag as additives in the cement manufacturing will contribute to a reduction of the CO<sub>2</sub> emissions.

According to literature, FNS concrete has favourable physical and chemical performances and high resistivity to chloride ion penetration (Komnitsas et al., 2009; Rahman et al., 2017). The application of slags in concrete opens up a whole range of new possibilities in the recycling of materials in the construction industry, while also reducing waste materials (Anastasiou et al., 2014). Furthermore, the incorporation of these materials could provide an added value to the cement properties. The FNS may also be used as building materials if the physicochemical characteristics are appropriate (Saha & Sarker, 2018b, 2019). In the last 50 years, studies showed that FNS are unsuitable for structural use (Ma et al., 2019; Olofinnade et al., 2016). Indeed, the valorisation of FNS in concrete has been limited to pelletised aggregates. Japan was ahead of establishing standards to use FNS in concrete aggregates or paving mixtures (Aba et al., 2010; JIS A 5011-2, 2016; JIS A 5015, 2013). Korea made a standard on FNS aggregates for concrete in the recent decades (KS F 2527, 2016). Aggregates must be inert. However, due to alkali-silicate reaction related to the silicate content in FNS, the use of high FNS content is still limited and there is no specification related to it (Saha & Sarker, 2016). Therefore, many researchers are suspicious of the FNS performance in cements as it was not proved in practice. However, in China performance-based research regarding its strength development was carried out (Mo et al., 2017; Wang et al., 2011, 2017) to use FNS as replacement of cement. Pozzolanic reaction was observed at blast furnace type of FNS (Mo et al., 2017), promoting the use of FNS as binder since the reactivity is necessary for hydration.

The FNS from New Caledonia is environmentally compatible for use in concrete due to a low amount of heavy metals leaching from it and still below the regulatory limits (Saha & Sarker, 2017).

However, in these previous studies, FNS was mainly used as a substitute material for concrete aggregates and a limited number of studies are available on the use of FNS from New Caledonia as supplementary cementitious materials unlike blast furnace slag or fly ash. Some problems have been encountered related to durability aspects (Saha et al., 2018; Saha & Sarker, 2018a, 2018b, 2020). Indeed, the presence of high proportion of magnesium oxide in FNS (>30%) is reducing its application as a supplementary cementitious material. This excess of MgO lead to deleterious expansion after 2 years of curing due to the hydration reaction of MgO (Du, 2005).

The FNS of this study are the waste product of nickel laterite ore processing, in particular, saprolite at the base of the laterite profile with low Al<sub>2</sub>O<sub>3</sub>, low Fe<sub>2</sub>O<sub>3</sub> and high MgO contents. This is of advantage, as the presence in a certain proportion of MgO and Al<sub>2</sub>O<sub>3</sub> in cements (binder) reduces shrinkage-cracking in mortar and concrete. This magnesium-rich cement can lead to an autogenous expansion at early curing times and can compensate the contraction of the concrete due to shrinkage (Du, 2005). In addition, the analyses of FNS by Saha and Sarker (2018a, 2018b, 2020) showed that magnesium is incorporated in these slags as crystalline forsterite (Mg<sub>2</sub>SiO<sub>4</sub>) and enstatite (Mg<sub>2</sub>SiO<sub>3</sub>). The crystalline structures of forsterite and enstatite are stable and chemically inert (Klein et al., 1998) and consequently do not participate to hydration reactions that produce expansion, e.g. Mg(OH)<sub>2</sub> (Kosanović et al., 2005; Maghsoudlou et al., 2016). Katsiotis et al. (2015) concluded that the presence of FNS slowed down the hydration process in FNS blended concretes. In addition, the authors reported an increase of compressive strength at later curing stages due to pozzolanic reaction effects of FNS. The consumption of portlandite by the pozzolanic reaction of FNS is considered as the first reason for the reduction of expansion.

In this study, we focus on the use of FNS as a supplementary cementitious materials. For that purpose, an experimental study of the soundness and compressive strength of specimens made with slags is carried out. Five mortar mixtures using different percentages of slags (0%, 5%, 10%, 15% and 20%) are cast and tested up to failure.

**Table 1.** XRF analysis of CEM I 42.5 N cement.

Oxide	SiO <sub>2</sub>	CaO	Al <sub>2</sub> O <sub>3</sub>	Fe <sub>2</sub> O <sub>3</sub>	MgO	SO <sub>3</sub>	K <sub>2</sub> O	Na <sub>2</sub> O	TiO <sub>2</sub>	Mn <sub>2</sub> O <sub>3</sub>	Loss on ignition
Concentration (wt.%)	20.1	61.4	5.2	4.3	1.9	2.9	1.5	0.9	0.1	0.1	1.6

Values in weight.%.

## 2. Materials and methods

### 2.1. Characterisation techniques

Elemental analysis of cement was performed using X-ray fluorescence spectroscopy using an Inel Equinox 3500 spectrometer, equipped with a Cu microfocus source, parabolic multilayer mirror on the primary beam, and an Amptek X-123SDD Silicon Drift Detector placed vertically 10 mm over the sample to ensure high sensitivity even with low-atomic number elements.

The FNS chemical analysis was performed at the SARM/CRPG laboratory, Nancy (France). The major elements were analysed by ICP-OES, while trace elements (As-Zr) were analysed by ICP-MS. Sulphur and CO<sub>2</sub> were analysed by infrared absorptiometry and FeO by volumetry. The detailed methods, detection limits and precisions of the analyses are presented in the SARM-CRPG website.

X-ray powder diffraction data was performed on a D8 Advance Vario 1 Bruker (two-circle diffractometer,  $\theta - 2\theta$  Bragg-Brentano mode) at room temperature and using a pure Cu K $\alpha$  radiation ( $\lambda = 1.54059 \text{ \AA}$ ) selected by an incident beam Ge (111) monochromator. Data are collected for  $2\theta$  varying from 15° to 100° for 2 s per 0.01° step (2 h scan<sup>-1</sup>). NIST SRM-660b LaB<sub>6</sub> standard powder was used to calibrate the instrumental contribution (Caglioti et al., 1958). Crystalline phase identification and quantification were performed using the Full-Pattern Search-Match procedure and the Crystallography Open Database (Grazulis et al., 2012). The Rietveld quantification was performed using the MAUD software (Lutterotti et al., 1997).

Raman spectroscopy was performed at room temperature with a Thermo Scientific DXR Raman microscope (Thermo Fisher Scientific Inc., Waltham, MA, USA) with a 532 nm laser as an excitation source. The Raman spectrometer is equipped with a 900 lines mm<sup>-1</sup> diffraction grating. A 50 $\times$  magnification long working distance objective was used to focus the laser beam onto the surface and collect the scattered light in a backscattering geometry. Data was collected over a range of 50–2200 cm<sup>-1</sup>. The spot size of the laser was estimated to 0.8  $\mu\text{m}$  and the spectral resolution to 3 cm<sup>-1</sup>. Raman spectra were systematically recorded twice at low laser power (1 mW) and with an integration time of 400 s. We used the Origin software and Lorentzian curves as elementary fitting functions for silica glass. The mineralogical compositions were determined by comparing the collected Raman spectra to those reported in the Raman Open Database ROD (El Mendili et al., 2019).

### 2.2. Materials and samples preparation

#### 2.2.1. Cement

The cement used in this study is a CEM I 42.5 N according to NF EN 197-1 standard (EN 197-1, 2001). The clinker ratio is 95–100%. The Blaine fineness is 3200 cm<sup>2</sup> g<sup>-1</sup>, and the density is 3.1 g cm<sup>-3</sup>. The chemical composition is given in Table 1.

#### 2.2.2. Sand

A natural silica sand (SiO<sub>2</sub> = 99 wt.%, H<sub>2</sub>O < 0.1%) made by Société Nouvelle du Littoral (French Source, Normalised sand, Certified Conform - EN 196-1 by the AFNOR and conforms to ISO 679) was used in this study. The sand grains are uncrushed and of rounded shape.

#### 2.2.3. Ferronickel slags

The FNS was provided by SLN (New Caledonia). The average particle size of the granulated slag is about 4 mm. Raw FNS is ground to powder (<63  $\mu\text{m}$ ) using high energy ball milling for 30 min (Figure 1). The specific gravity of the slag is 2.9, which is slightly lower than that of cement (~3.1).

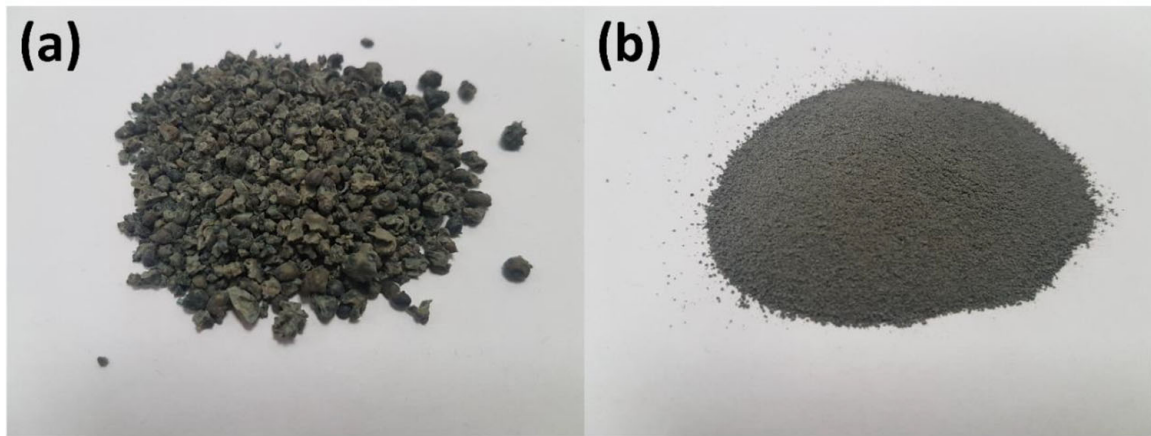


**Figure 1.** (a) Raw (4 mm) and (b) ground FNS (< 63 microns).

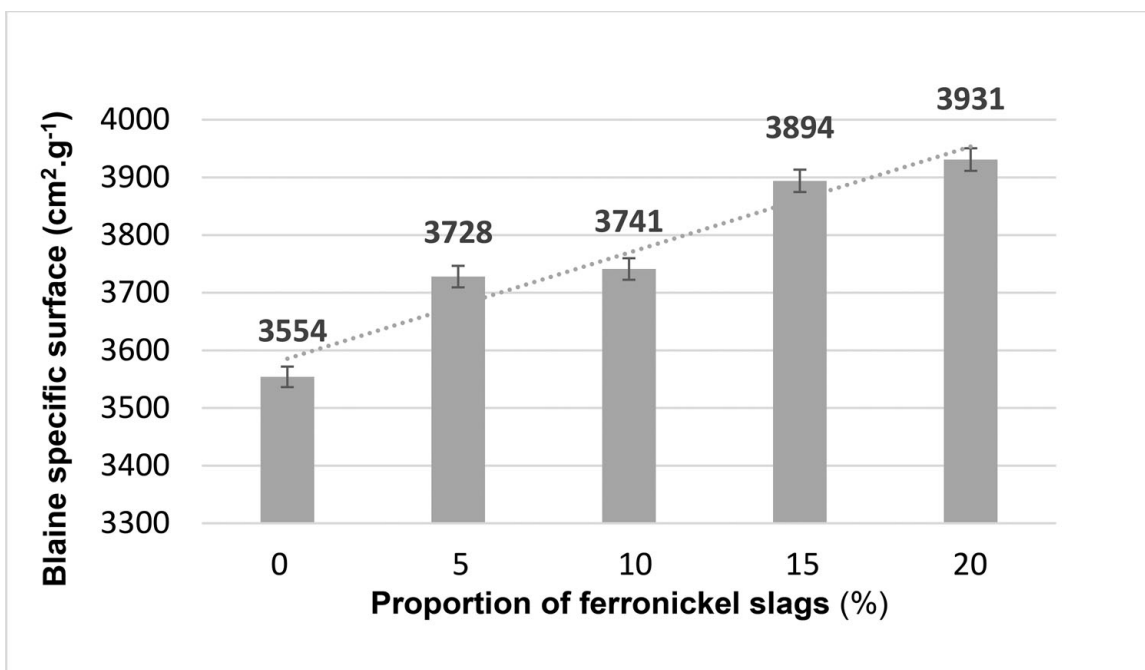


**Figure 2.** Evolution of the Blaine SSA of the cements elaborated with a proportion of FNS in conventional cement. Error bars are standard deviation calculated for 3 replicates.

#### 2.2.4. Slag cement mixture

The FNS addition increases the Blaine specific surface area (SSA) of the cement powder (Figure 2). This phenomenon is due to a much larger specific surface of FNS compared to cement ( $6700 \text{ cm}^2 \text{ g}^{-1}$  for FNS and  $3554 \text{ cm}^2 \text{ g}^{-1}$  for cement). However, this SSA increase is not a simple linear combination (Figure 2, dashed line) of the two constituting SSAs, indicating that some blockage of the initial specific surface of FNS by mixing with cement occurs. This blockage is neatly visible at 5% FNS probably due to less FNS particle contact during mixing for such low amounts.

#### 2.2.5. Mortars composition

Mortars used in this study are elaborated with a water to cement ratio (W/C) fixed to 0.5, and a sand to cement ratio at 3 (Table 2). After mixing, the mortars were cast in three layers into square prism moulds ( $40 \times 40 \times 160 \text{ mm}$ ) according to EN 196-1 (Regourd, 1980). The moulds were then placed in a controlled temperature room ( $20 \pm 1 \text{ }^\circ\text{C}$ ) at 90% of relative humidity. The mortar specimens were demoulded 24 h after manufacturing, and then conserved in water at  $20 \pm 1 \text{ }^\circ\text{C}$  until the time of experiments.

It is important to notice that we limit the replacement level of cement by FNS to 20%. Indeed, when using higher substitution levels of cement by FNS (>20%), compressive and flexural strengths decreased dramatically, and the slump flow is very reduced.

**Table 2.** Mortars composition.

Sample	Mass substitution rate of cement by FNS (%)
CM	0
M-FNS5	5
M-FNS10	10
M-FNS15	15
M-FNS20	20

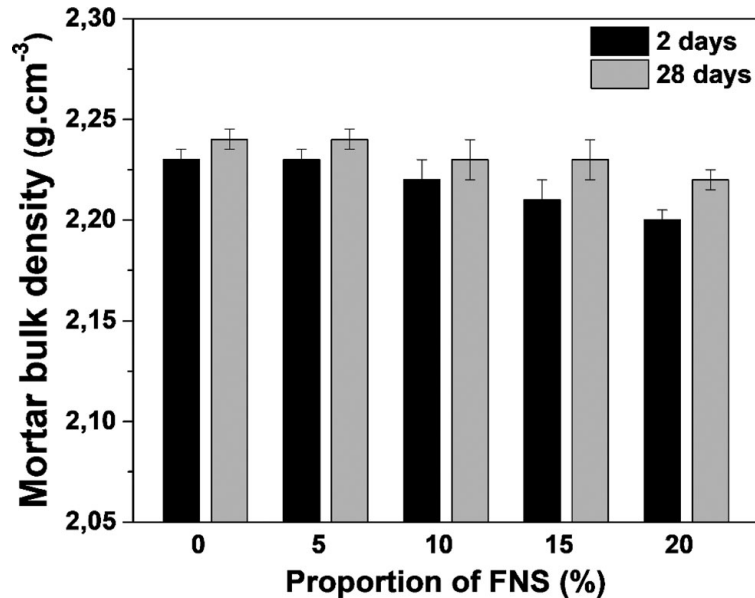


**Figure 3.** Variation of the bulk density of the mortars elaborated with different substitution of cement by FNS after 2 days (black) and after 28 days of aging (grey).

An increase in the bulk density for all mixes is observed with increasing curing time up to 28 days (Figure 3). Increasing the slag content gradually decreases mortar density at all aging times compared to the control mortar. Since the FNS density is slightly lower than that of the ordinary cement, such an overall decrease with FNS incorporation could be interpreted as a sole effect. However, the decrease is more significant after 2 days than after 28 days. This indicates further densification during curing time for larger FNS contents.

### 2.3. Experimental methods

#### 2.3.1. Fresh properties of mortars

Workability experiments were carried out on fresh mortar within the French standard NF P18-452. The experimental device consists of a compartment divided into two unequal volumes by a removable wall. The test measures the time taken for the mortar to flow from the large compartment to the smaller one under the influence of an imposed vibration.

The initial and final setting times were also measured for each mortar. These experiments consist in measuring the time necessary for a plunger assembly with a total weight of 1000 g to penetrate into the material. The initial setting time is effective when the distance between the end of plunger and the base-plate is 2.5 mm according to the NF P 15-431 standard.

#### 2.3.2. Mechanical properties of hardened mortars

Mechanical properties of the mortars were measured using compressive and three-point bending tests in accordance to the EN 196-1 standard, on all samples from 2 to 28 days of aging. The compression tests used a loading rate of 40 N min<sup>-1</sup> while 3-points bending tests were displacement-controlled at a rate of 0.07 mm min<sup>-1</sup>.



**Table 3.** Chemical composition of FNS (wt.%) obtained by ICP-MS and ICP-OES normalised to most stable oxides.

Oxide	(wt.%)	Element	ppm	Element	ppm	Element	ppm	Element	ppm
SiO <sub>2</sub>	51.67	As	<d.l	Hf	0.22	Ta	0.06	Nd	1.48
Al <sub>2</sub> O <sub>3</sub>	2.29	Ba	16.24	In	<d.l	Th	0.44	Sm	0.34
Fe <sub>2</sub> O <sub>3</sub> (FeO)	12.58 (11.3)	Be	0.24	Mo	2.15	U	0.16	Eu	0.08
MnO	0.46	Bi	<d.l	Nb	0.38	V	65	Gd	0.36
MgO	31.56	Cd	<d.l	Ni	665	W	d.l	Tb	0.06
CaO	0.31	Co	61	Pb	1.34	Y	3.31	Dy	0.41
Na <sub>2</sub> O	0.50	Cr	7932	Rb	1.41	Zn	236	Ho	0.09
K <sub>2</sub> O	0.03	Cs	0.17	Sb	0.22	Zr	8.37	Er	0.27
TiO <sub>2</sub>	0.04	Cu	9.19	Sc	24	La	1.53	Tm	0.05
P <sub>2</sub> O <sub>5</sub>	<d.l	Ga	0.63	Sn	0.45	Ce	2.49	Yb	0.29
Total	99.44	Ge	0.16	Sr	13	Pr	0.37	Lu	0.05

d.l.: detection limit.

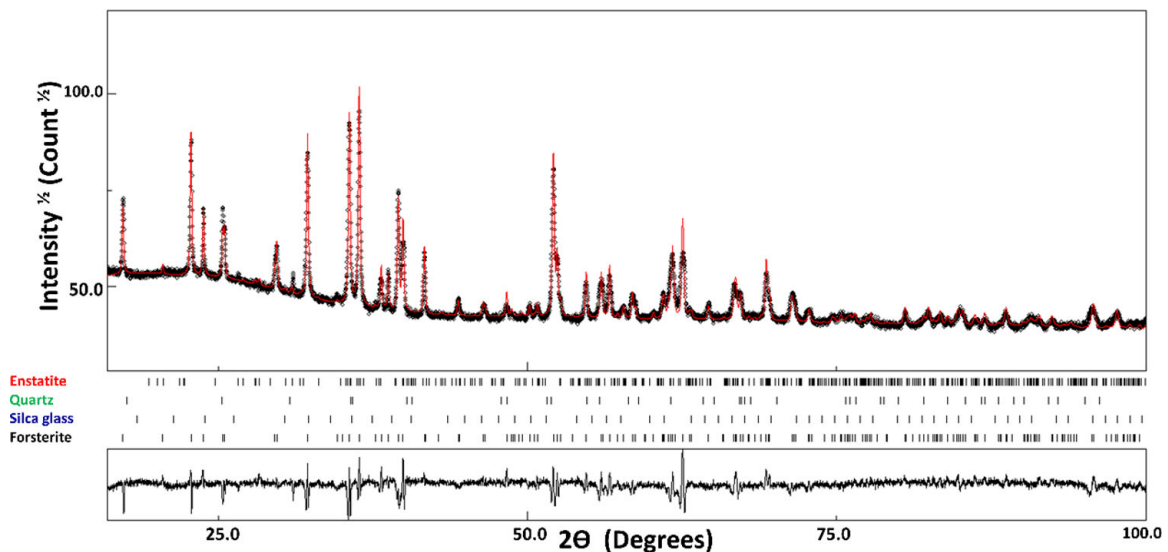


**Figure 4.** X-ray diffraction pattern of a ground FNS sample refined using the MAUD software. The calculated pattern (red line) is superimposed on the observed profile (coarse line). The difference curve ( $I_{obs} - I_{calc}$ ) is shown at the bottom.

### 3. Results and discussion

#### 3.1. Microstructural characterisation of FNS

Table 3 shows the elemental compositions of the used bulk FNS powder after grinding. The slag sample is mainly composed of about 52 wt.% of SiO<sub>2</sub>, 32 wt.% of MgO and 12.6 wt.% of total iron reported as Fe<sub>2</sub>O<sub>3</sub>. In this latter, the iron majority is divalent (FeO: 11.3 wt.%). Minor compounds are 2.3 wt.% Al<sub>2</sub>O<sub>3</sub>, about 0.5 wt.% of Na<sub>2</sub>O and MnO, 0.3 wt.% of CaO and 0.4 wt.% total H<sub>2</sub>O. CO<sub>2</sub> is at low contents (0.16 wt.%) and K<sub>2</sub>O and TiO<sub>2</sub> are below 0.04 wt.%.

An XRD pattern of the FNS sample can reasonably be refined using four main phases (Figure 4 and Table 4). Quantitative phase analysis using Rietveld refinement indicates quartz and forsterite as the two major phases.

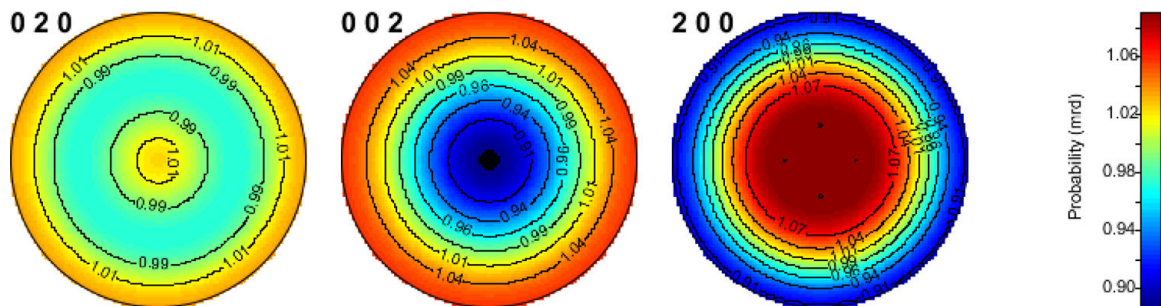
The weighted profile R-factor ( $R_{wp}$ ) = 3.2% and the Bragg R-factor ( $R_B$ ) = 2.2% and the Goodness of the Fits < 2 (GoF = 1.68) are reasonably low and ensure quantitative estimates of the phases and their microstructural properties.

The hexagonal closed-packed array of oxygen anions, stacked along the  $\vec{a}$  direction in the structure of forsterite, is expanded and distorted compared to usual ones (Bragg & Brown, 1926; Smyth et al., 2000). Such oxygen anions occupy three different crystallographic sites, with O1 and O2 on a mirror plane and O3 in a general position. The oxygens bound to octahedral and tetrahedral cations to each other (3 and 1, respectively; Brown, 1982). Mg cations occupy Mg1 and Mg2 octahedral sites, while Si cations occupy tetrahedral sites. Mg octahedra share their edges and corners, and only corners with isolated SiO<sub>4</sub> tetrahedra, resulting in more distorted and larger Mg2 sites compared to Mg1. Due to X-ray scattering contrasts, only Ni substitution of Mg could be probed by refinements.

**Table 4.** Refined values of lattice parameters, unit cell volume, average diameter, microstrain  $\langle \varepsilon^2 \rangle^{1/2}$ , model used and the atom occupancies.

Phases	COD reference	Volume (%)	Lattice type + space group	Lattice parameters (Å)	Average diameter: $\langle D \rangle$ (nm)	Microstrain $\langle \varepsilon^2 \rangle^{1/2}$ (r.m.s.)	Texture and atoms
Forsterite $\text{Mg}_2\text{SiO}_4$	9000319	29.4 (3)	Orthorhombic Pbnm	$a = 4.743$ (1) $b = 10.181$ (1) $c = 5.950$ (2)	523 (20)	$6 \cdot 10^{-4}$	<b>Texture:</b> Harmonic <b>Occupancies:</b> Mg1: 98.3% Ni1: 1.7% Mg2: 99.6% Ni2: 0.4%
Enstatite $\text{Mg}_2\text{SiO}_3$	9014117	3.2 (2)	Orthorhombic Pbca	$a = 18.595$ (1) $b = 8.794$ (1) $c = 5.235$ (1)	254 (13)	$1 \cdot 10^{-3}$	
$\text{SiO}_2$	1011097	13.5 (4)	Cubic P213	$a = 9.401$ (1)	120 (10)	0	
Quartz	9000594	50.9 (7)	Trigonal P3 <sub>2</sub> 21	$a = 5.633$ (2) $c = 5.240$ (2)	95 (7)	$1 \cdot 10^{-4}$	

Standard deviations are indicated in parenthesis on the last digit.

**Figure 5.** Pole figures of forsterite.

Divalent cations ( $\text{Ca}^{2+}$ ,  $\text{Mn}^{2+}$  and  $\text{Ni}^{2+}$ ) may substitute Mg in natural olivines thanks to similar ionic radii. In the case of nickel, the liebenbergite solid solution  $(\text{Mg,Ni})_2\text{SiO}_4$  is formed (McDonald & Whittington, 2008), inducing a small cell parameter decrease compared to pure forsterite, due to the smaller octahedral ionic radius of  $\text{Ni}^{2+}$  ( $r_{\text{Mg}^{2+}} = 0.71 \text{ \AA}$  and  $r_{\text{Ni}^{2+}} = 0.69 \text{ \AA}$ ; Zhang et al., 2015).

In order to be able to accurately reproduce diffracted intensities of the Ni-bearing forsterite (liebenbergite), it was necessary to use a texture model for this phase despite the fact that its texture strength is low with a maximum orientation density of the  $\{200\}$  pole figure around 1.1 m.r.d (Figure 5). We used a harmonic texture model as implemented in Maud, included in the Rietveld fit. The refined texture corresponds to  $\vec{a}$  axes perpendicular to the sample plane, with the  $\vec{c}/\vec{b}$  axes at random around  $\vec{a}$ , i.e. a  $\langle 200 \rangle$  fibre texture component.

The refined unit-cell parameters of Ni-bearing forsterite are  $a = 4.743(1) \text{ \AA}$ ,  $b = 10.181(1) \text{ \AA}$  and  $c = 5.950(2) \text{ \AA}$ , while those expected for pure forsterite are  $a = 4.75$ ,  $b = 10.20$  and  $c = 5.98 \text{ \AA}$  (Smyth & Hazen, 1973), indicating clearly the cell parameters decrease. With  $\vec{c}$  axes parallel to the edge-sharing octahedral Mg1-Mg1-Mg1 chain, modification of the Mg1 octahedron size significantly influences the  $\vec{c}$  cell parameter (Boström, 1987), as indicated from our fits, with a smaller effect along  $\vec{a}$  due to unoccupied every second octahedral chain in this direction (Boström, 1987).

Resulting occupancies are (in at.%): 98.3 Mg + 1.7Ni in the Mg1 sites and 99.6 Mg + 0.4Ni in the Mg2 sites (Table 4). The Mg2 sites are larger than the Mg1 sites in forsterite, which implies that the larger  $\text{Mg}^{2+}$  cations (compared to  $\text{Ni}^{2+}$ ) tend to occupy the larger Mg2 sites in olivine.

In summary, the XRD diagram of the FNS is dominated by quartz (50.9%), Ni-bearing forsterite  $(\text{Ni,Mg})_2\text{SiO}_4$  (29.4%), silica (13.5%) and enstatite (3.2%). These phases were identified in each slag powder batch independently of their particle size.

Raman spectroscopy analyses confirm that the FNS slags are polycrystalline and heterogeneous whose main components are amorphous silica ( $\text{SiO}_2$ ), quartz ( $\text{SiO}_2$ ), forsterite  $(\text{Mg,Ni})_2\text{SiO}_4$  and enstatite  $(\text{Mg,Fe})_2\text{SiO}_3$  with some traces of Akaganeite ( $\beta\text{-FeO}_{1-2x}(\text{OH})_1 + x\text{Cl}_x$ ), chromite ( $\text{FeCr}_2\text{O}_4$ ), calcite ( $\text{CaCO}_3$ ; Figures 6 and 7). Forsterite is a highly stable mineral with a melting point of  $1890 \text{ }^\circ\text{C}$  (Kosanović et al.,

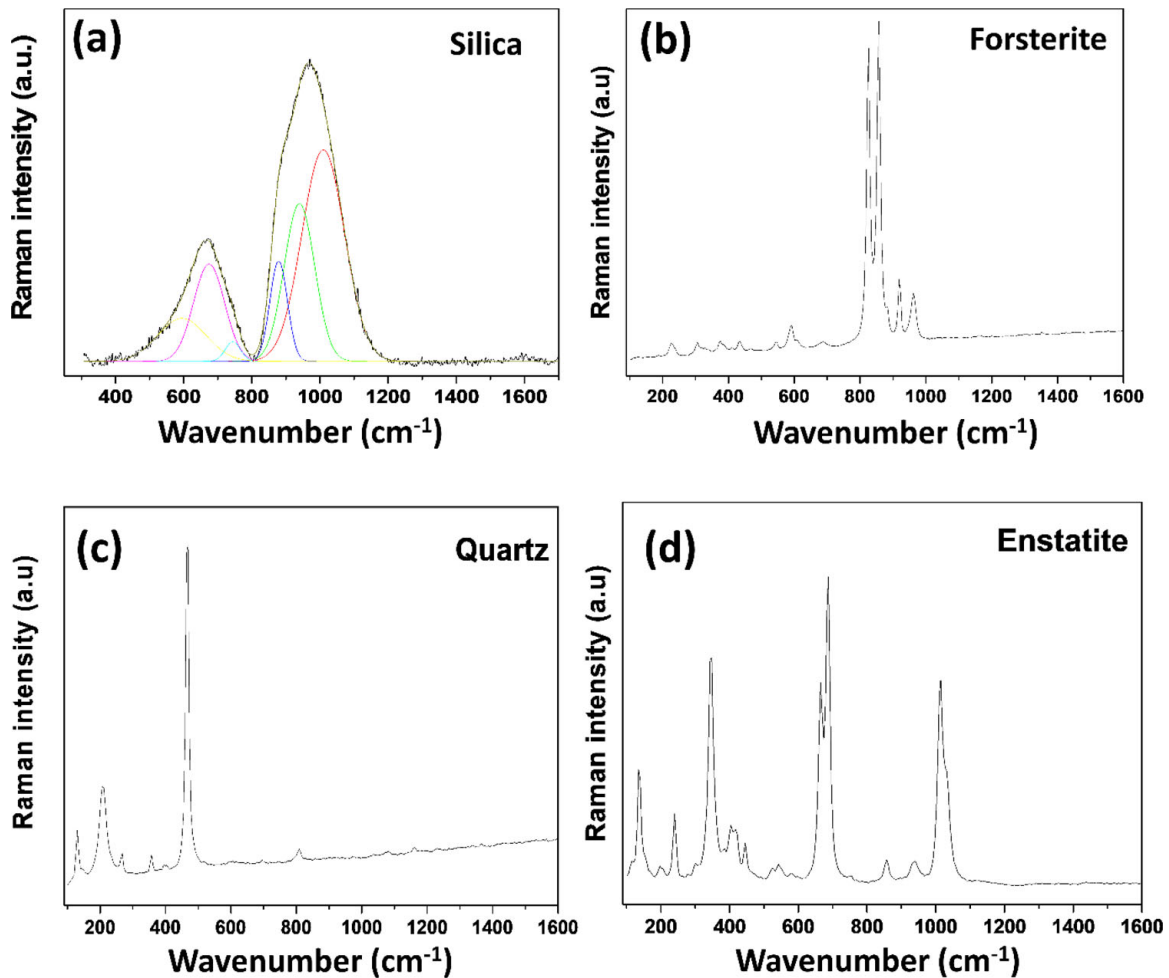


**Figure 6.** Raman spectrum of: (a) silica deconvoluted with six Gaussians, (b) forsterite, (c) quartz and (d) enstatite.

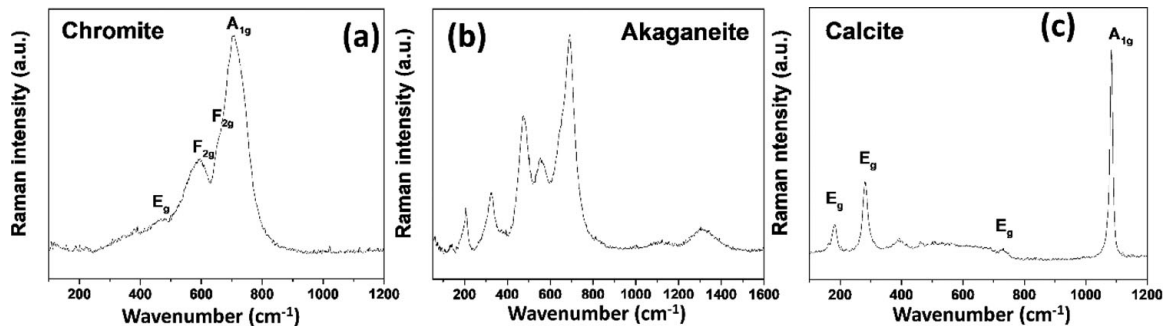


**Figure 7.** Raman spectrum of (a) chromite, (b) akaganeite and (c) calcite.

2005; Maghsoudlou et al., 2016). It is known that periclase (MgO) reacts with amorphous silica at temperatures above 900 °C to form forsterite (Kosanović et al., 2005). In the presence of high quantity of quartz and silica, forsterite reacts with SiO<sub>2</sub> to form enstatite (Michel et al., 2014).

### 3.1.1. Phases detected by XRD and Raman spectroscopy

The Raman analysis has been successfully applied to a large variety of vitrified glass as encountered in the field of nuclear waste management. The structure of the silicate network in a glass is mainly determined by the degree of the silicate tetrahedra polymerisation and described by the abundance of different  $Q_n$  species, where  $Q_n$  referred to a tetrahedron linked by bridging oxygen atoms to  $n$  adjacent tetrahedra. The range of  $n$  is 0 (corresponding to isolated tetrahedra) to 4 (corresponding to fully polymerised three-dimensional network).  $Q_0$  is the isolated monomer,  $Q_1$  and  $Q_2$  are chains and  $Q_3$  and  $Q_4$  reflect the interconnected structures.



**Table 5.** Refined centres for Gaussian functions for the Raman spectrum of silica.

Peaks	Vibration mode	Centre
1	$Q_3$	1010
2	$Q_2$	940
3	$Q_1$	880
4	Si-O stretching	750
5	O—(Ca, Mg, Si)—O bending	675
6	O—(Mg, Si)—O bending	595

Figure 6(a) shows the spectrum obtained for the glassy-like silica structure. The best refinement of the Raman spectrum is obtained with six Gaussians (Table 5).

The Raman spectrum of amorphous silica is composed of broad peaks corresponding to the vibration modes of the  $Q_1$ ,  $Q_2$  and  $Q_3$  species present at 880, 940 and 1010  $\text{cm}^{-1}$ , respectively. The broad band at 595  $\text{cm}^{-1}$  is assigned to the vibration twisting and stretching modes of the Si-O-Si bonds (Galeener, 1982; Matson et al., 1983; McMillan, 1984). Other contributions are present in the spectrum, such as the vibration mode at 675  $\text{cm}^{-1}$  attributed to a poorly crystalline calcium-magnesium silicate (Deng et al., 2002; Martinez-Ramirez et al., 2006). The band at 750  $\text{cm}^{-1}$  is assigned to Si-O stretching vibration with a dominant Si motion (Matson et al., 1983). The relative proportion of  $Q_3/Q_2$  is high, indicating enhancement in the number of  $Q_3$  silicon sites and a high degree of polymerisation. This finding is important for using this material as a cement additive. The above described structure implies a higher degree of stiffness, strength and density of the silicate over time. In general, a higher degree of polymerisation in amorphous structures leads to higher compressive strengths (Ma et al., 2019; Wu et al., 2017). In addition, it is known that a magnesium-rich binder can lead to early strength development and durability of cementitious materials (Zhang et al., 2014).

Olivine phases have 81 optical modes but only 36 of which are Raman active ( $11A_g + 11 B_{1g} + 7B_{2g} + 7B_{3g}$ ; Take, 1978). For forsterite (Figure 6(b)), the bands in the 800 and 1100  $\text{cm}^{-1}$  range are attributed to  $\text{SiO}_4$  internal stretching vibrational modes. The features observed in that region are a doublet with peaks at 818 and 848  $\text{cm}^{-1}$  whose relative intensities are function of the crystal orientation. These vibration bands result from the coupled asymmetric and symmetric vibrations of  $\text{SiO}_4$  tetrahedra. The bands in the 400–800  $\text{cm}^{-1}$  wavenumber region correspond to the  $\text{SiO}_4$  internal bending vibrational modes. Bands below 400  $\text{cm}^{-1}$  are contributed by lattice modes and dominated by the rotations of  $\text{SiO}_4$  tetrahedra and translations of octahedral coordinated cations (magnesium motion) in the crystal lattice (Chopelas, 1991; Kolesov & Geiger, 2004). The Raman spectrum of the forsterite present in FNS is slightly different compared to pure forsterite phase, with all Raman vibration modes slightly shifted towards lower wavenumbers (Table 6). The vibration bands shift is in agreement with the tendency observed in Ni-bearing forsterite for a small amount of Ni substituting Mg (El Mendili et al., 2019). This result is consistent with the one obtained by XRD with 2.2% of  $\text{Mg}^{2+}$  replaced by  $\text{Ni}^{2+}$  in octahedral sites (Figure 4 and Table 4).

Quartz crystals are formed in silica-rich slags during cooling and solidification. The Raman spectrum of such crystals (Figure 6(c)) shows the strong Raman modes of  $\alpha$ -quartz (462  $\text{cm}^{-1}$ ) corresponding to symmetric stretching of oxygen of six-membered  $\text{SiO}_4$  tetrahedra,  $\nu_s(\text{Si-O-Si})$  (Lin, 2004). In addition, the Raman spectrum shows the lattice modes of quartz at 206  $\text{cm}^{-1}$ . Raman bands in the frequency range up to 300  $\text{cm}^{-1}$  correspond to complex translations and rotations of the  $\text{SiO}_4$  tetrahedra. Raman bands in the high-wavenumber range (805  $\text{cm}^{-1}$ ) are assigned to the Si-O stretching motions within tetrahedral  $\text{SiO}_4$  units.

Usually, orthopyroxene enstatite exhibits three ranges of Raman spectrum signatures (Figure 6(d)): (1) non-bridging and bridging Si-O modes between 970 and 1070  $\text{cm}^{-1}$  and 850 and 950  $\text{cm}^{-1}$ , respectively; (2) bending Si-O modes between 500 and 600  $\text{cm}^{-1}$  and (3) bending and stretching metal-oxygen modes. Stretching vibration bands are assigned in the 970–1070  $\text{cm}^{-1}$  range, related to the non-bridging Si-O bonds (Farmer, 1974; McMillan, 1984; McMillan & Hofmelster, 1988; Sharma et al., 1983). The 650–750  $\text{cm}^{-1}$  range corresponds to the Si-O stretching modes of the bridging O atoms while the bending O-Si-O modes are present in the 500–600  $\text{cm}^{-1}$  range. In addition, two Mg-O (375–500  $\text{cm}^{-1}$ ) and Fe-O octahedron vibration modes (225–350  $\text{cm}^{-1}$ ) may appear.

### 3.1.2. Phases only detected by Raman spectroscopy

Chromite (Figure 7(a)) exhibits four bands for Fe-O and Cr-O bond-stretching (Reddy & Frost, 2005). The broad and very intense band at 790  $\text{cm}^{-1}$  is due to symmetric stretching  $A_{1g}(\nu_1)$ , while the two bands at

**Table 6.** Raman vibration modes of Ni-bearing forsterite present in the FNS compared to those of forsterite and the Ni end member, liebenbergite and their symmetries and assignments.

Symmetries and assignments (Lin, 2001)	Forsterite (Martinez-Ramirez et al., 2006; Regourd, 1980)	Liebenbergite (Lin, 2001; Wang et al., 2004)	Ni-forsterite (FNS)
$B_{1g}$ T(SiO <sub>4</sub> , MO <sub>6</sub> :y)	192	165 ± 2	sh
$A_g$ T(SiO <sub>4</sub> , MO <sub>6</sub> :y)	226 ± 2	–	221 ± 2 m
$B_{2g}$ T(SiO <sub>4</sub> :z)	243 ± 1	–	sh
$A_g$ T(MO <sub>6</sub> , SiO <sub>4</sub> :x)	305 ± 2	248 ± 2	–
$B_{2g}$ R(SiO <sub>4</sub> :x)	324 ± 2	–	321 ± 3 vw
$A_g$ T(MO <sub>6</sub> :y)	330 ± 1	–	–
$B_{2g}$ R(SiO <sub>4</sub> :y)	366 ± 3	295	299 ± 2 w
$B_{3g}$ R(SiO <sub>4</sub> :z)	375 ± 1	328	326 ± 3 vw
$B_{1g}$ T(MO <sub>6</sub> )	383	336	368 ± 3 vw
$B_{1g}$ $\nu_2$	435 ± 3	387	433 ± 2 w
$B_{1g}$ $\nu_4$	545 ± 2	516 ± 1	526 ± 2 w
$B_{3g}$ $\nu_4$	593 ± 3	552 ± 3	585 ± 2 m
$B_{1g}$ $\nu_4$	632	573	597 ± 3 vw
$A_g$ $\nu_1$	825 ± 1	811 ± 1	818 ± 1 vs
$A_g$ $\nu_3$	856 ± 1	837 ± 1	848 ± 1 vs
$B_{1g}$ $\nu_3$	882 ± 3	–	876 ± 2 m
$B_{1g}$ $\nu_3$	921 ± 1	885 ± 3	912 ± 1 s
$A_g$ $\nu_3$	966 ± 2	928 ± 2	949 ± 1 s

The symmetries and assignments are based on those reported in literature for forsterite and liebenbergite.

T: translation; R: rotation;  $\nu_1$ : symmetric stretching;  $\nu_2$ : symmetric deformation;  $\nu_3$ : asymmetric stretching;  $\nu_4$ : asymmetric deformation.

sh: should be present, vw: very weak, w: weak, m: medium, s: strong and vs: very strong.

730 and 485 cm<sup>-1</sup> are attributed to  $F_{2g}(\nu_4)$  and  $E_g(\nu_2)$ , respectively, and the broad band at 590 cm<sup>-1</sup> to the  $F_{2g}(\nu_3)$  mode.

Figure 7(b) shows Raman bands around 308, 390, 535 and 720 cm<sup>-1</sup>, characteristic for Akaganeite (El Mendili et al., 2014). Akaganeite ( $\beta$ -FeO<sub>1-2x</sub>(OH)<sub>1+x</sub>Cl<sub>x</sub>) is often observed as a corrosion product of carbon steel in marine environments (Monnier et al., 2010), and always contains Cl<sup>-</sup> ions. As shown by Keller, Akaganeite can contain up to 6 wt.% chloride (Keller, 1969). It is also preferentially formed compared to lepidocrocite and goethite in environments with high concentration of Fe<sup>2+</sup> and Cl<sup>-</sup>. The presence of Akaganeite in FNS results probably from the cooling of slag with seawater. Akaganeite can accommodate up to 19 wt.% of nickel in its structure (Buckwald & Clark, 1989). We did not perform Raman spectroscopy to prove nickel substitution in akaganeite.

Figure 7(c) illustrates the Raman spectrum of calcite. The strong Raman band at 1088 cm<sup>-1</sup> is assigned to the  $A_{1g}$  mode. Its internal  $E_g$  mode is observed at 712 cm<sup>-1</sup> and its external  $E_g$  or lattice modes occur at 282 and 156 cm<sup>-1</sup> (Ait Chaou et al., 2015).

In summary, the composition of FNS are dominated by quartz, forsterite, silicate and enstatite.

The use of the pozzolanic materials have increased in recent years. Indeed, pozzolanic materials are generally able to react with the hydrated calcium hydroxide forming the hydrated calcium silicate (C–S–H) responsible for the strength of hydrated cement pastes. The XRD analysis shows the presence of nano-sized crystals of quartz (=95 nm), and thus, quartz cannot be considered as a chemically inert material (Benezet & Benhassaine, 1999a, 1999b). The pozzolanic reaction of quartz is not linked to the vitreous structure of the particles in reaction but to a dissolution-precipitation reaction of particles (Benezet & Benhassaine, 1999a, 1999b). It is barely perceptible for the particle diameters exceeding a certain critical size (>5µm) and the reduction in particle diameter will lead to a large rise in particle reactivity. Quartz, when mixed in certain proportions, improves the properties of both fresh and hard concrete such as durability, permeability and compressive, flexural and tensile strengths (Lin et al., 2018). The presence of silica glass with a high degree of polymerisation can also lead to higher compressive strength (Ma et al., 2019; Wu et al., 2017). In addition, it is known that magnesium-rich binder can lead to early strength development and durability of cementitious materials (Zhang et al., 2014).

All these results show the potential of FNS additive for producing a mortar with high performance.

### 3.2. Fresh state mortar properties

Our results show that slag incorporation has no effect on the flow times for all slag-cement compositions. Indeed, all samples present a good flow time with values between 7 and 9 s. The water amount required

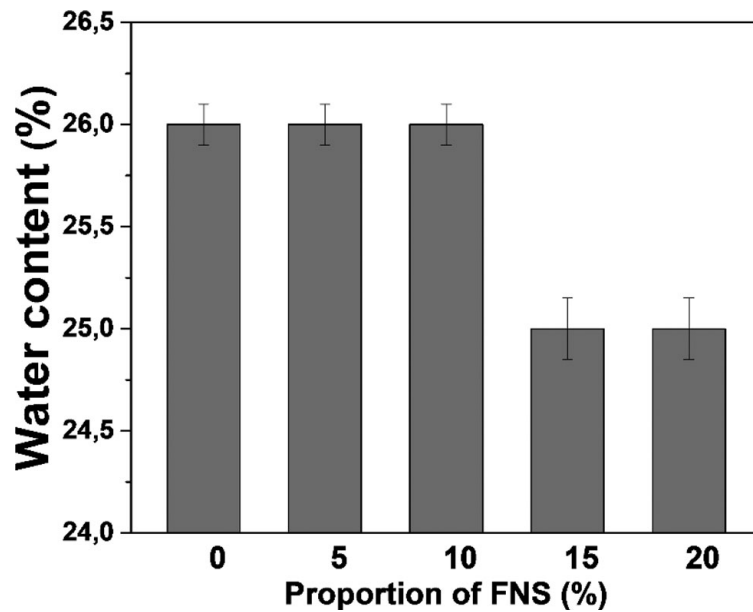


Figure 8. Water contents for normal consistency of cement paste with different concentrations of FNS.

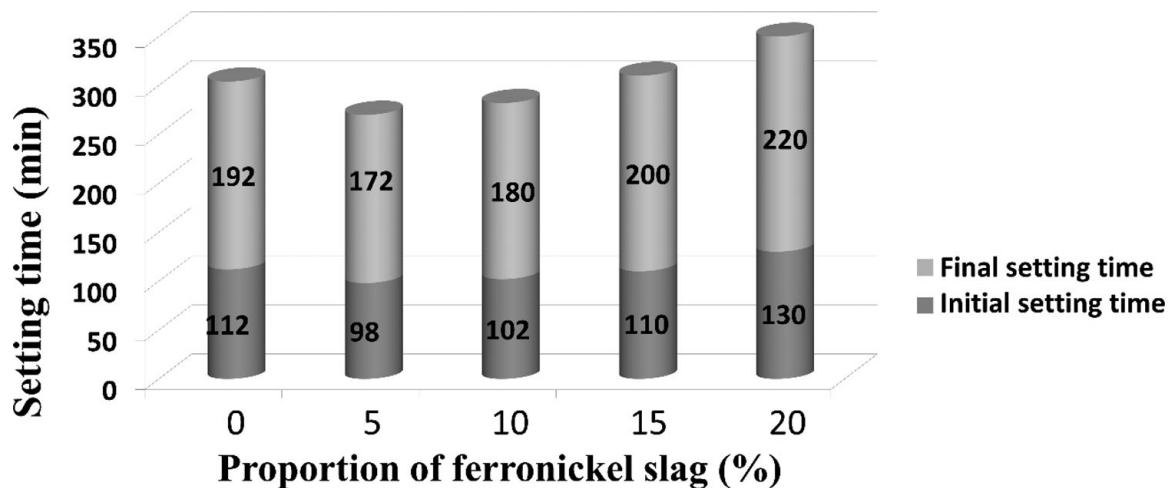


Figure 9. Initial and final setting times of the different mortars.

for the paste normal consistency slightly decreased with the inclusion of FNS (Figure 8), from around 26% of water up to 10% of FNS to around 25% for larger FNS incorporation. Consequently, the water to solid ratio (W/S) requirement of the control mix is larger than those of the mixes containing 15% and 20% FNS by a factor 1.08, indicating an 8% lower water consumption for the largest FNS mix. The water requirements of FNS are comparable to those of other supplementary cementitious materials, such as fly ash and blast furnace (Sobolev et al., 2018). The observed decrease in water requirement is due to a lower rate of slag hydration attributed to its mineralogical composition, to the presence of quartz with its low reactivity and to the amorphous silica with its high degree of polymerisation. Cement substitution by slag also reduces the amount of ettringite produced during early stages of hydration which is responsible for improvement in flowability (Sobolev et al., 2018).

Compared to the control sample, FNS-incorporated samples exhibit gradual increase in initial and final setting times (Figure 9). While these times decrease by 10% as soon as 5% of FNS is added, it reduces to 5% at 10% FNS, and becomes larger than for the control sample at larger FNS contents.

The addition of up to 10% of slags accelerates the setting time. With 15% slag replacement, the setting time is almost equivalent to that of the control specimen and beyond 15%, the initial and final setting times are extended.

Given the fixed environmental factors and the use of the same cement type, we can conclude that different setting times are the result of slag and hence reduction of the hydration rate. Indeed, the increased percentage of cement substitution by FNS increases the separation distance between hydrated

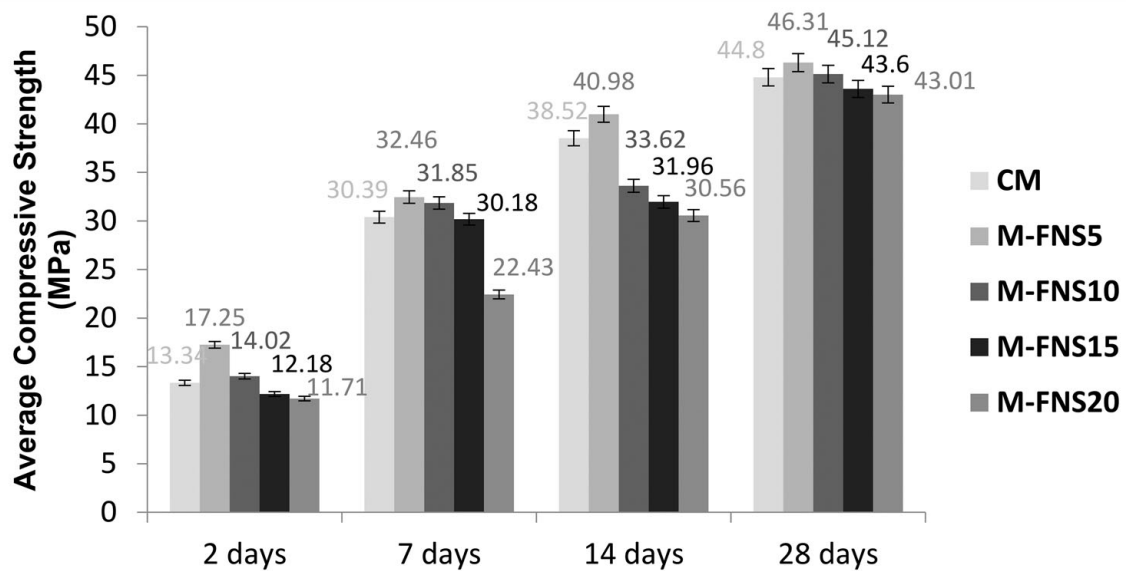


**Figure 10.** Compressive strength values of the mixtures at different ages.

cement particles, delaying then the formation of interlocking network between the particles (Lizarazo-Mariaga et al., 2011). It is important to note that FNS has a very low (0.31 wt.%) calcium content. Thus, the setting time is increased at a high percentage of cement replacement by the low calcium-containing FNS.

Replacement of less than 20 percent of FNS does not affect setting times significantly. The setting time values of all samples are in accordance with the NF EN 196-3 standard, which confirms the results obtained by the normal consistency test. At cement substitution of about 20% by FNS it was found that this latter delays both the initial and the final setting times by 18 and 28 min, respectively, compared to that of the control mix. The slight improvement at 5% and 10%, is probably due to the synergetic effect and mutual activation when compound mineral admixtures of slag powder are mixed with cement into mortar. Long setting times are usually avoided for common applications of concrete because of increased time of formwork.

### 3.3. Compressive and flexural strength of mortar

The compressive strengths of mortars after curing times of 2, 7, 14 and 28 days are shown in Figure 10. Whatever the considered formulation, the compressive strength increases with the age of the specimens. At a FNS incorporation of 10%, the compressive strength decreases. However, the compressive strength values of FNS mortars are very close at 28 and 90 days, regardless of the substitution rate, and are above 43 MPa. The maximum compressive strength values are obtained at 5% FNS for all curing times. Slag seems to act more at short curing times. Indeed, the compressive strength for the 5% FNS mortar increases, over the one of the control mortar, by 29% and 4%, respectively at 2 and 28 days. At a low replacement ratio (up to 10%), an increase in non-evaporable water occurs at an early age due to the filler effect and later because of slag hydration. For higher replacement rates, the filler effect cannot compensate for the dilution effect caused by the large incorporation of slow reacting slag particles (Castellano et al., 2016).

Figure 11 shows that the flexural tensile strengths are lower at substitution rates up to 15%. This phenomenon is due to the relatively slow pozzolanic reactivity of FNS (Papadakis et al., 2002), since it contains a high weight fraction of SiO<sub>2</sub>. However, as for compressive strength and for all curing times, the flexural tensile strengths of the specimen with 5% of slags are larger than those of other mixes including the control mix. The flexural tensile strengths at 2 and 28 days for the 5% FNS mortar increase compared to the control mortar by 16% and 5%, respectively.

These results are consistent with those obtained for the setting time. In fact, the hydration process is accelerated at a low incorporation of 5% of FNS. This increases the mechanical strength, especially at short curing times.

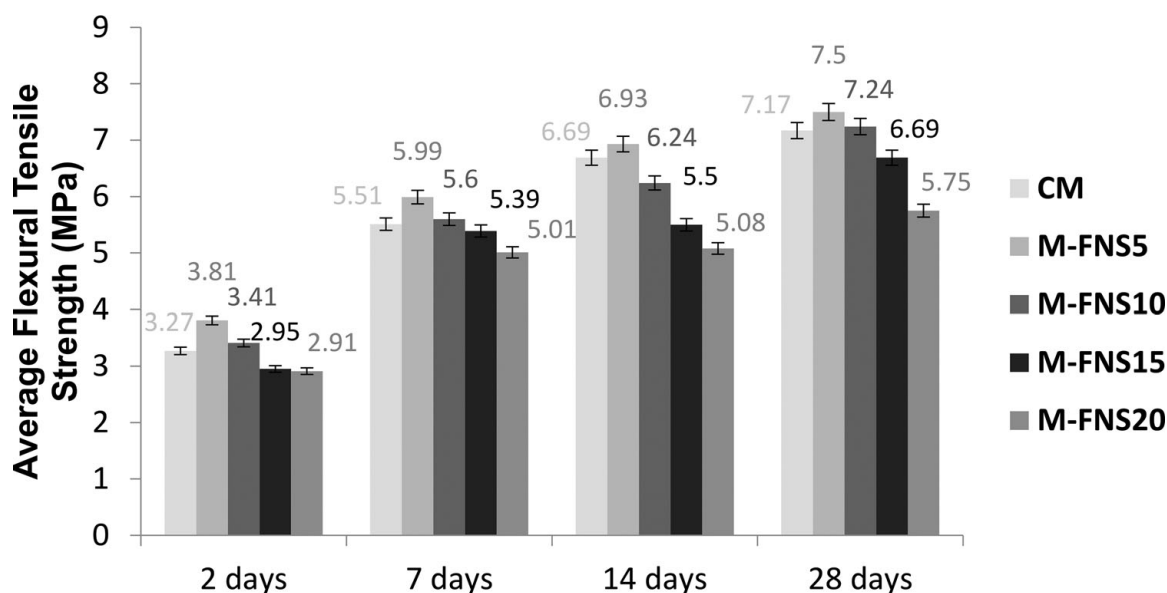


Figure 11. Flexural tensile strength of the mixes at different curing times.

The flexural strength of the different mortars correlates positively with the compressive strength. The kinetics of hardening between 2 and 28 days is the same for all specimens. The maximum flexural strength values are measured at 5% slag replacement level. The difference between these strengths and those obtained for the control mortar tends to decrease with the age of the specimens. However, the flexural strength of the 5% FNS remains larger than or equal to that of the control mortar at 28 days. It is 7.5 and 7.2 MPa, respectively.

It is important to notice that there is a significant increase in compressive strength of M-FNS5, M-FNS10, M-FNS15 and M-FNS20 specimens, compared to the CM between the 28th and the 90th days (not shown here). This confirms the pozzolanic effect of the FNS.

In order to achieve larger flexural and compressive strengths, the use of FNS powder at low substitution ratio (between 5% and 10%) is recommended.

At high substitution levels (>10%), the low flexural and tensile strengths are mainly attributed to the slow FNS pozzolanic activity, FNS being rich in  $\text{SiO}_2$ . This phenomenon is explained by the interaction between the reactive silica, the amorphous part of the FNS, representing 13.5% and the  $\text{Ca}(\text{OH})_2$  released by the cement hydration. The pozzolanic reaction is not predominant at short curing times. Therefore, intense hydration at young ages induces low strengths.

The results at 28 days curing time show that replacing 5% of cement by FNS, improved the compressive and flexural strengths (Figures 10 and 11). The larger compaction potential is due to the difference in particle sizes. The fine quartz and amorphous particle sizes (between 95 and 120 nm) amounting to 64.4 wt.% in the FNS slag, fill voids between the cement particles. This results in dense packing and also enhances pozzolanic reaction of silica particles.

However, when increasing the amount of  $\text{SiO}_2$  powder (both amorphous and crystalline silica) above 5-10%, the compressive and flexural strengths are reduced. This is particularly due to the increase in non-pozzolanic  $\text{SiO}_2$  powder particles.

The optimum of 20% FNS replacement ratio is consistent with literature finding including the study by Rahman et al. (2017), where the compressive strength value after 28 days of curing matched that of control mortar. The compressive strength development of the FNS was found comparable to those of other commonly used supplementary cementitious materials such as fly ash or ground-granulated blast-furnace slag (GGBF). For the fly ash (containing 62% of  $\text{SiO}_2$ ), Celik et al. (2015) showed that, the mechanical strengths of mortars containing up to 20% of fly ash remain close to those of the control mortar. With the increase of the fly ash content, it is globally observed a decrease of the compressive and flexural strengths.

Mohamed (2018) studied the substitution of cement by GGBF (containing 34% of  $\text{SiO}_2$ ) up to 80%. The results showed that the mixes in which cement was replaced with 10% to 60% GGBS matched or exceeded the 28-day compressive strength of the control mix.



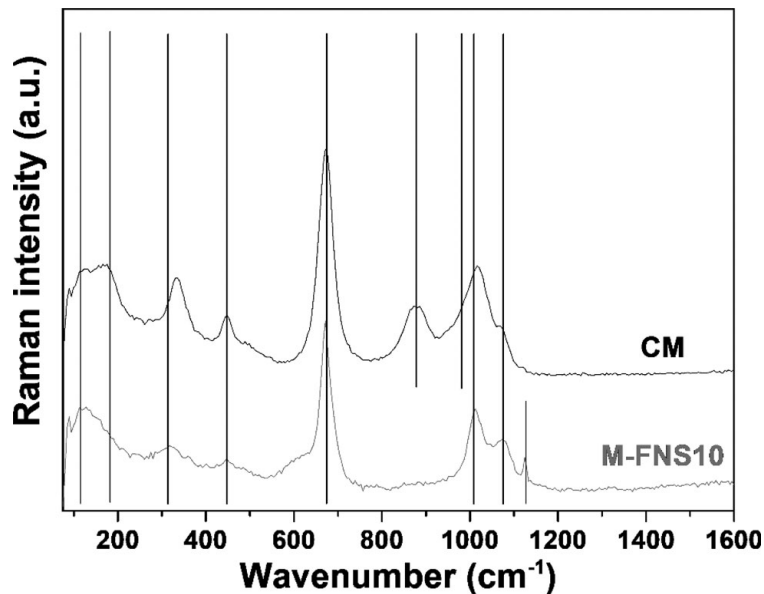


**Figure 12.** Raman spectrum of the C-S-H present on the mortars surface after 28 days of aging: (a) ordinary mortar, (b) M-FNS10 mortar.

### 3.4. Analyses of mortars by Raman spectroscopy

The Raman analyses of the mortar surface (ordinary mortar and M-FNS10) after 28 days of aging show the presence of C-S-H (Figure 12). All mortar samples (not shown here) exhibit the presence of calcite.

The Raman spectra of C-S-H systems were widely studied (Garbev et al., 2007; Kirkpatrick et al., 1997). The most intense band at  $670\text{ cm}^{-1}$  is attributed to Si-O stretching. At low wavenumbers ( $100\text{--}360\text{ cm}^{-1}$ ) the lattice vibrations of the Ca-O polyhedra are observed. The band at  $445\text{ cm}^{-1}$  is due to twisting and stretching of Si-O-Si. Bands in the  $850\text{--}1200\text{ cm}^{-1}$  range are associated to the symmetric stretching modes of  $Q_n$  species in silicate (Si-O).

Comparing the Raman spectra of C-S-H formed in the ordinary mortar and in the M-FNS10, we can notice a significant decrease of the Ca-O polyhedra intensities and bandwidth. This behaviour is due to the low calcium-content (0.31 wt.%) in FNS. The Raman spectra of the C-S-H shows a decrease of  $Q_1$  ( $880\text{--}890\text{ cm}^{-1}$ ) and an increase of  $Q_3$  ( $1080\text{ cm}^{-1}$ ) for the M-FNS10 mortar compared to the control. This difference can be interpreted by silica layers cross linking in this sample. The  $Q_2$  modes ( $1000\text{--}1020\text{ cm}^{-1}$ ) are also observed as a split into two main bands at  $1006$  and  $1015\text{ cm}^{-1}$ . This result confirms the modification of the Si-O-Si chain length by a change of the quantity of silica tetrahedron with  $Q_{2p}$  (pairing) and  $Q_{2b}$  (bridging) components (Grangeon et al., 2016). In addition, the Raman analysis shows the formation of an additional band at  $1130\text{ cm}^{-1}$  in M-FNS10, which is attributed to the formation of the reticulated  $\text{SiO}_2$  networks  $Q_4$ , and indicates a higher polymerisation degree of the silica chains in the C-S-H structure. The greater effectiveness of FNS is attributed to its higher silica content. The high silica content of FNS of about 52 wt.%, produces more C-S-H gel as a result of pozzolanic reaction. This leads to a porosity reduction and consequently to the increase in strength. Moreover, magnesium-rich binder are known to lead to early strength development and durability of cementitious materials (Zhang et al., 2014).

## 4. Conclusion

The effects of cement replacement by FNS on the cement paste and mortar properties were studied at different percentages. All results show that using FNS cement in mortar can improve the mortar performance. The introduction of FNS at a rate up to 10% accelerates the setting. The addition of FNS at 5% increases the compressive and flexural strengths of mortars. It is suggested that FNS can be used over this threshold, up to 20%, as a partial substitute for cement in production of mortar if a moderate of mechanical strength is acceptable. For SLN, this represents 2 million of tons of annual waste potential recycling, with around an actual stockpile of 25 million of tons straightfull available. Our results demonstrate a real potential for the use of these slags in the composition of cementitious materials.

Extrapolating this number to world's yearly cement production scale (4.6 billion of tons), 920 million of tons of FNS can be recycled as cement additives. The substitution of cement by FNS contributes to sustainable development and 'green deal' goals, due to less use of cement and a significant reduction in CO<sub>2</sub> emissions.

## Acknowledgement

ERAMET-SLN is thanked for providing the FNS from New Caledonia.

## Disclosure statement

No potential conflict of interest was reported by the authors.

## ORCID

Daniel Chateigner  <http://orcid.org/0000-0001-7792-8702>

Yassine El Mendili  <http://orcid.org/0000-0001-7061-855X>

## References

- Aba, M., Sakoi, Y., Shoya, M., Tsukinaga, Y., & Nagataki, S. (2010). Properties of concrete incorporating ferromagnetic slag as coarse aggregates. *Concrete Research and Technology*, 21(3), 63–75. [https://doi.org/10.3151/crt.21.3\\_63](https://doi.org/10.3151/crt.21.3_63)
- Ait Chaou, A., Abdelouas, A., El Mendili, Y., Bouakkaz, R., Utsunomiya, S., Martin, C., & Bourbon, X. (2015). Vapor hydration of a simulated borosilicate nuclear waste glass in unsaturated conditions at 50 °C and 90 °C. *RSC Advances*, 5(79), 64538–64549. <https://doi.org/10.1039/C5RA12384D>
- Anastasiou, E., Filikas, K. G., & Stefanidou, M. (2014). Utilization of fine recycled aggregates in concrete with fly ash and steel slag. *Construction and Building Materials*, 50, 154–161. <https://doi.org/10.1016/j.conbuildmat.2013.09.037>
- Ashok, D. D., Gordon Bacon, W., & Robert, O. C. (2004). The Past and the Future of Nickel Laterites, In *PDAC 2004 International Convention, Trade Show, Investors Exchange* (p. 18), March 7–10. [https://scholar.google.com/scholar\\_lookup?hl=en&volume=1-7&publication\\_year=2004&author=+Dalviaauthor=D+Ashokauthor=W+Gordon+Baconauthor=Robert+C+Osborne&title=The+Past+and+The+Future+of+Nickel+Laterites](https://scholar.google.com/scholar_lookup?hl=en&volume=1-7&publication_year=2004&author=+Dalviaauthor=D+Ashokauthor=W+Gordon+Baconauthor=Robert+C+Osborne&title=The+Past+and+The+Future+of+Nickel+Laterites)
- Benezet, J. C., & Benhassaine, A. (1999a). Grinding and pozzolanic reactivity of quartz powders. *Powder Technology*, 105(1–3), 167–171. [https://doi.org/10.1016/S0032-5910\(99\)00133-3](https://doi.org/10.1016/S0032-5910(99)00133-3)
- Benezet, J. C., & Benhassaine, A. (1999b). The influence of particle size on the pozzolanic reactivity of quartz. *Powder Technology*, 103(1), 26–29. [https://doi.org/10.1016/S0032-5910\(99\)00010-8](https://doi.org/10.1016/S0032-5910(99)00010-8)
- Boström, D. (1987). Single-crystal X-ray diffraction studies of synthetic Ni-Mg olivine solid solutions. *American Mineralogist*, 72, 965–972.
- Bragg, W. L., & Brown, G. B. (1926). Die Struktur des Olivins. *Zeitschrift für Kristallographie*, 63, 538–556.
- Brown, G. E. (1982). Olivines and silicate spinels. In P. H. Ribbe (Ed.), *Orthosilicates* (p. 275). Mineralogical Society of America.
- Buckwald, V. F., & Clark, R. (1989). Corrosion of Fe-Ni alloys containing akaganeite: The Antarctic Meteorite case. *American Mineralogist*, 74, 656–676.
- Caglioti, G., Paoletti, A., & Ricci, F. P. (1958). Choice of collimators for a crystal spectrometer for neutron diffraction. *Nuclear Instruments*, 3(4), 223–228. [https://doi.org/10.1016/0369-643X\(58\)90029-X](https://doi.org/10.1016/0369-643X(58)90029-X)
- Castellano, C. C., Bonavetti, V. L., Donza, H. A., & Irassar, E. F. (2016). The effect of w/b and temperature on the hydration and strength of blastfurnace slag cements. *Construction and Building Materials*, 111, 679–688. <https://doi.org/10.1016/j.conbuildmat.2015.11.001>
- Celik, K., Meral, C., Gursel, A. P., Mehta, P. K., Horvath, A., & Monteiro, P. J. (2015). Mechanical properties, durability, and life-cycle assessment of self-consolidating concrete mixtures made with blended Portland cements containing fly ash and limestone powder. *Cement and Concrete Composites*, 56(56), 59–72. <https://doi.org/10.1016/j.cemconcomp.2014.11.003>

- Chopelas, A. (1991). Single crystal Raman spectra of forsterite, fayalite, and monticellite. *American Mineralogist*, 76, 1101–1109.
- Deng, C.-S., Breen, C., Yarwood, J., Habesch, S., Phipps, J., Craster, R., & Maitland, G. (2002). Ageing of oil-field cement at high humidity: A combined FEG-ESEM and Raman microscopic investigation. *Journal of Materials Chemistry*, 12(10), 3105–3112. <https://doi.org/10.1039/b203127m>
- Du, C. (2005). A review of magnesium oxide in concrete. *Concrete International*, 27 (12), 45–50.
- El Mendili, Y., Abdelouas, A., Ait Chaou, A., Bardeau, J.-F., & Schlegel, M. L. (2014). Carbon steel corrosion in clay-rich environment. *Corrosion Science*, 88, 56–65. <https://doi.org/10.1016/j.corsci.2014.07.020>
- El Mendili, Y., Chateigner, D., Orberger, B., Gascoin, S., Bardeau, J.-F., Petit, S., Duée, C., Le Guen, M., & Pilliere, H. (2019). Combined XRF, XRD, SEM-EDS and Raman analyses on serpentinized harzburgite (Nickel laterite mine, New Caledonia): Implications for exploration and geometallurgy. *ACS Earth and Space Chemistry*, 3(10), 2237–2249. <https://doi.org/10.1021/acsearthspacechem.9b00014>
- El Mendili, Y., Vaitkus, A., Merkys, A., Gražulis, S., Chateigner, D., Mathevet, F., Gascoin, S., Petit, S., Bardeau, J.-F., Zanatta, M., Secchi, M., Mariotto, G., Kumar, A., Cassetta, M., Lutterotti, L., Borovin, E., Orberger, B., Simon, P., Hehlen, B., & Le Guen, M. (2019). Raman Open Database: First interconnected Raman-X-ray diffraction open-access resource for material identification. *Journal of Applied Crystallography*, 52(Pt 3), 618–625. <https://doi.org/10.1107/S1600576719004229>
- EN 197-1. (2001). Ciment - Partie 1: Composition, spécifications et critères de conformité des ciments courants, AFNOR.
- Farmer, V. C. (1974). Orthosilicate, pyrosilicates, and other finite-chain silicates. In V. C. Farmer (Ed.), *The infrared spectra of minerals* (pp. 285–303). Mineralogical Society of London.
- Galeener, F. L. (1982). Planar rings in vitreous silica. *Journal of Non-Crystalline Solids*, 49(1–3), 53–62. [https://doi.org/10.1016/0022-3093\(82\)90108-9](https://doi.org/10.1016/0022-3093(82)90108-9)
- Garbev, K., Stemmermann, P., Black, L., Breen, C., Yarwood, J., & Gasharova, B. (2007). Structural features of C-S-H(I) and its carbonation in air-A Raman spectroscopic study. Part I: Fresh phases. *Journal of the American Ceramic Society*, 90(3), 900–907. <https://doi.org/10.1111/j.1551-2916.2006.01428.x>
- Grangeon, S., Claret, F., Roosz, C., Sato, T., Gaboreau, S., & Linard, Y. (2016). Structure of nanocrystalline calcium silicate hydrates: Insights from X-ray diffraction, synchrotron X-ray absorption and nuclear magnetic resonance. *Journal of Applied Crystallography*, 49(3), 771–783. <https://doi.org/10.1107/S1600576716003885>
- Gražulis, S., Daškevič, A., Merkys, A., Chateigner, D., Lutterotti, L., Quirós, M., Serebryanaya, N. R., Moeck, P., Downs, R. T., & Le Bail, A. (2012). Crystallography Open Database (COD): An open-access collection of crystal structures and platform for world-wide collaboration. *Nucleic Acids Research*, 40(Database issue), D420–D427. <https://doi.org/10.1093/nar/gkr900>
- Ibrahim, E., Barnabé, P., Ramanaidou, E., & Pirard, E. (2018). Mapping mineral chemistry of a lateritic outcrop in New Caledonia through generalized regression using Sentinel-2 and field reflectance spectra. *International Journal of Applied Earth Observation and Geoinformation*, 73, 653–665. <https://doi.org/10.1016/j.jag.2018.08.004>
- JIS A 5011-2. (2016). Slag aggregate for concrete - Part 2: Ferronickel slag aggregate. Japanese Industrial Standards Committee.
- JIS A 5015. (2013). Iron and steel slag for road construction. Japanese Industrial Standards Committee.
- Katsiotis, N. S., Tsakiridis, P. E., Velissariou, D., Katsiotis, M. S., Alhassan, S. M., & Beazi, M. (2015). Utilization of ferronickel slag as additive in Portland cement: A hydration leaching study. *Waste and Biomass Valorization*, 6(2), 177–189. <https://doi.org/10.1007/s12649-015-9346-7>
- Keller, P. (1969). Vorkommen, Entstehung und Phasenumwandlung von  $\beta$ -FeOOH in Rost. *Materials and Corrosion/Werkstoffe und Korrosion*, 20(2), 102–108. <https://doi.org/10.1002/maco.19690200205>
- Kirkpatrick, R. J., Yarger, J. L., McMillan, P. F., Ping, Y., & Cong, X. (1997). Raman spectroscopy of C-S-H, tobermorite, and jennite. *Advanced Cement Based Materials*, 5(3–4), 93–99. [https://doi.org/10.1016/S1065-7355\(97\)00001-1](https://doi.org/10.1016/S1065-7355(97)00001-1)
- Klein, C., Hurlbut, C. S., & Dana, J. D. (1998). *Manual of mineralogy* (21st ed., pp. 373–375). Wiley.
- Kolesov, B. A., & Geiger, C. A. (2004). A Raman spectroscopic study of Fe-Mg olivines. *Physics and Chemistry of Minerals*, 31(3), 142–154. <https://doi.org/10.1007/s00269-003-0370-y>
- Komnitsas, K., Zaharaki, D., & Perdikatsis, V. (2009). Effect of synthesis parameters on the compressive strength of low-calcium ferronickel slag inorganic polymers. *Journal of Hazardous Materials*, 161(2–3), 760–768. <https://doi.org/10.1016/j.jhazmat.2008.04.055>

- Kosanović, C., Stubičar, N., Tomašić, N., Bermanec, V., & Stubičar, M. (2005). Synthesis of a forsterite powder by combined ball milling and thermal treatment. *Journal of Alloys and Compounds*, 389(1–2), 306–309. <https://doi.org/10.1016/j.jallcom.2004.08.015>
- KS F 2527. (2016). Crushed aggregate for concrete. Korean Standard Association.
- Lin, C. C. (2001). High-pressure Raman spectroscopic study of Co- and Ni-olivines. *Physics and Chemistry of Minerals*, 28(4), 249–257. <https://doi.org/10.1007/s002690100158>
- Lin, C. C. (2004). Pressure-induced polymorphism in enstatite (MgSiO<sub>3</sub>) at room temperature: Clinoenstatite and orthoenstatite. *Journal of Physics and Chemistry of Solids*, 65(5), 913–921. <https://doi.org/10.1016/j.jpccs.2003.09.028>
- Lin, R. S., Wang, X. Y., & Zhang, G. Y. (2018). Effects of quartz powder on the microstructure and key properties of cement paste. *Sustainability*, 10(10), 3369. <https://doi.org/10.3390/su10103369>
- Lizarazo-Marriaga, J., Claisse, P. A., & Ganjian, E. (2011). Effect of steel slag and Portland cement in the rate of hydration and strength of blast furnace slag pastes. *Journal of Materials in Civil Engineering*, 23(2), 153–160. [https://doi.org/10.1061/\(ASCE\)MT.1943-5533.0000149](https://doi.org/10.1061/(ASCE)MT.1943-5533.0000149)
- Lutterotti, L., Matthies, S., Wenk, H. R., Schultz, A. S., & Richardson, J. W. (1997). Combined texture and structure analysis of deformed limestone from time-of-flight neutron diffraction spectra. *Journal of Applied Physics*, 81(2), 594–600. <https://doi.org/10.1063/1.364220>
- Ma, H., Zhu, H., Yi, C., Fan, J., Chen, H., Xu, X., & Wang, T. (2019). Preparation and reaction mechanism characterization of alkali-activated coal gangue–slag materials. *Materials*, 12(14), 2250. <https://doi.org/10.3390/ma12142250>
- Ma, Z., Tang, Q., Yang, D., & Ba, G. (2019). Durability studies on the recycled aggregate concrete in china over the past decade: A review. *Advances in Civil Engineering*, 2019, 1–19. <https://doi.org/10.1155/2019/4073130>
- Maghsoudlou, M. S. A., Ebadzadeh, T., Sharafi, Z., Arabi, M., & Zahabi, K. R. (2016). Synthesis and sintering of nano-sized forsterite prepared by short mechanochemical activation process. *Journal of Alloys and Compounds*, 678, 290–296. <https://doi.org/10.1016/j.jallcom.2016.02.020>
- Martinez-Ramirez, S., Frías, M., & Domingo, C. (2006). Micro-Raman spectroscopy in white Portland cement hydration: Long-term study at room temperature. *Journal of Raman Spectroscopy*, 37(5), 555–561. <https://doi.org/10.1002/jrs.1428>
- Matson, D. W., Sharma, S. K., & Philpotts, J. A. (1983). The structure of high-silica alkali-silicate glasses. A Raman spectroscopic investigation. *Journal of Non-Crystalline Solids*, 58(2–3), 323–352. [https://doi.org/10.1016/0022-3093\(83\)90032-7](https://doi.org/10.1016/0022-3093(83)90032-7)
- McDonald, R. G., & Whittington, B. I. (2008). Atmospheric acid leaching of nickel laterites review. Part I. Sulphuric acid technologies. *Hydrometallurgy*, 91(1–4), 35–55. <https://doi.org/10.1016/j.hydromet.2007.11.009>
- McMillan, P. (1984). Structural studies of silicate glasses and melts-applications and limitations of Raman spectroscopy. *American Mineralogist*, 69, 622–644.
- McMillan, P. (1984). Structural studies of silicate glasses and melts: Applications and limitations of Raman spectroscopy. *American Mineralogist*, 69, 633–644.
- McMillan, P. F., & Hofmelster, A. M. (1988). Infrared and Raman spectroscopy. *Mineralogical Society of America Reviews in Mineralogy*, 18, 99–159.
- Michel, R., Ammar, M. R., Simon, P., de Bilbao, E., & Poirier, J. (2014). Behaviour of olivine refractories at high temperature: Agglomeration in a fluidized bed reactor. *Refractories: Worldforum*, 6, 95–98.
- Mo, L., Zhang, F., Deng, M., Jin, F., Al-Tabbaa, A., & Wang, A. (2017). Accelerated carbonation and performance of concrete made with steel slag as binding materials and aggregates. *Cement and Concrete Composites*, 83, 138–145. <https://doi.org/10.1016/j.cemconcomp.2017.07.018>
- Mohamed, O. (2018). Durability and compressive strength of high cement replacement ratio self-consolidating concrete. *Buildings*, 8(11), 153. <https://doi.org/10.3390/buildings8110153>
- Monnier, J., Neff, D., Réguer, S., Dillmann, P., Bellot-Gurlet, L., Leroy, E., Foy, E., Legrand, L., & Guillot, I. (2010). A corrosion study of the ferrous medieval reinforcement of the Amiens cathedral. Phase characterisation and localisation by various microprobes techniques. *Corrosion Science*, 52(3), 695–710. <https://doi.org/10.1016/j.corsci.2009.10.028>
- Nickel, L. (2017). *SLN, FNS: A promising construction material for the Pacific Region*. <http://sln.nc/sites/default/files/flippingbook/slnslg/fichiers/assets/common/downloads/publicati622on.pdf>.



- Olofinnade, O. M., Ede, A. N., Ndambuki, J. M., & Bamigboye, G. O. (2016). Structural properties of concrete containing ground waste clay brick powder as partial substitute for cement. *Materials Science Forum*, 866, 63–67. <https://doi.org/10.4028/www.scientific.net/MSF.866.63>
- Papadakis, V. G., Antiohos, S., & Tsimas, S. (2002). Supplementary cementing materials in concrete. Part II: A fundamental estimation of the efficiency factor. *Cement and Concrete Research*, 32(10), 1533–1538. [https://doi.org/10.1016/S0008-8846\(02\)00829-3](https://doi.org/10.1016/S0008-8846(02)00829-3)
- Rahman, M. A., Sarker, P. K., Shaikh, F. U. A., & Saha, A. K. (2017). Soundness and compressive strength of Portland cement blended with ground granulated ferronickel slag. *Construction and Building Materials*, 140, 194–202. <https://doi.org/10.1016/j.conbuildmat.2017.02.023>
- Reddy, B. J., & Frost, R. L. (2005). Spectroscopic characterization of chromite from the Moa-Baracoa Ophiolitic Massif, Cuba. *Spectrochimica Acta, Part A, Molecular and Biomolecular Spectroscopy*, 61(8), 1721–1728. <https://doi.org/10.1016/j.saa.2004.07.002>
- Regourd, M. (1980). Structure and behaviour of slag Portland cement hydrates. Proceedings of 7th ICCO Paris France, I, III 2/10-12/26, 1980.
- Saha, A. K., & Sarker, P. K. (2016). Expansion due to alkali-silica reaction of ferronickel slag fine aggregate in OPC and blended cement mortars. *Construction and Building Materials*, 123, 135–142. <https://doi.org/10.1016/j.conbuildmat.2016.06.144>
- Saha, A. K., & Sarker, P. K. (2017). Sustainable use of ferronickel slag fine aggregate and fly ash in structural concrete: Mechanical properties and leaching study. *Journal of Cleaner Production*, 162, 438–448. <https://doi.org/10.1016/j.jclepro.2017.06.035>
- Saha, A. K., & Sarker, P. K. (2018a). Durability characteristics of concrete using ferronickel slag fine aggregate and fly ash. *Magazine of Concrete Research*, 70(17), 865–874. <https://doi.org/10.1680/jmacr.17.00260>
- Saha, A. K., & Sarker, P. K. (2018b). Durability of mortar incorporating ferronickel slag aggregate and supplementary cementitious materials subjected to wet-dry cycles. *International Journal Concrete Structures and Materials*, 12(1), 29. <https://doi.org/10.1186/s40069-018-0264-5>
- Saha, A. K., & Sarker, P. K. (2019). Mitigation of the potential alkali-silica reaction of FNS using ground FNS as a supplementary binder. *Advances in Cement Research*, 1–27. <https://doi.org/10.1680/jadcr.19.00035>
- Saha, A. K., & Sarker, P. K. (2020). Effect of sulphate exposure on mortar consisting of ferronickel slag aggregate and supplementary cementitious materials. *Journal of Building Engineering*, 28, 101012. <https://doi.org/10.1016/j.jobbe.2019.101012>
- Saha, A. K., Khan, M. N. N., & Sarker, P. K. (2018). Value added utilization of by-product electric furnace ferronickel slag as construction materials: A review. *Resources, Conservation & Recycling*, 134, 10–24. <https://doi.org/10.1016/j.resconrec.2018.02.034>
- Sharma, S. K., Simons, B., & Yoder, H. S. Jr (1983). Raman study of anorthite: Calcium Tschermak's pyroxene and gehlenite in crystalline and glassy states. *American Mineralogist*, 68, 1113–1125.
- Smyth, J. R., & Hazen, R. M. (1973). The crystal structures of forsterite and hortonolite at several temperatures up to 900 °C. *American Mineralogist*, 58, 588–593.
- Smyth, J. R., Jacobsen, S. D., & Hazen, R. M. (2000). Comparative crystal chemistry of orthosilicate minerals. In R. M. Hazen and R. T. Downs (Eds.), *High-temperature and high-pressure crystal chemistry* (Vol. 41, pp. 187–209). Reviews in Mineralogy and Geochemistry, Mineralogical Society of America.
- Sobolev K., Kozhukhova M., Sideris K., Menéndez E., & Santhanam M. (Eds.) (2018). Alternative supplementary cementitious materials. In *Properties of fresh and hardened concrete containing supplementary cementitious materials: State-of-the-art report of the RILEM technical committee 238-SCM Working Group 4* (Vol. 25, pp. 233–282). Springer International Publishing.
- Take, H. (1978). Growth of fayalite (Fe<sub>2</sub>SiO<sub>4</sub>) single crystals by the floating-zone method. *Journal of Crystal Growth*, 43, 463–468.
- The European Cement Association (CEMBUREAU). (2017). Activity Report (1st ed., pp. 1–42). CEMBUREAU.
- Wang, A., Kuebler, K., Jolliff, B., & Haskin, L. A. (2004). Mineralogy of a Martian meteorite as determined by Raman spectroscopy. *Journal of Raman Spectroscopy*, 35(6), 504–514. <https://doi.org/10.1002/jrs.1175>
- Wang, Q., Wang, D., & Zhuang, S. (2017). The soundness of steel slag with different free CaO and MgO contents. *Construction and Building Materials*, 151, 138–146. <https://doi.org/10.1016/j.conbuildmat.2017.06.077>



- Wang, Q., Yan, P., & Feng, J. (2011). A discussion on improving hydration activity of steel slag by altering its mineral compositions. *Journal of Hazardous Materials*, 186(2–3), 1070–1075. <https://doi.org/10.1016/j.jhazmat.2010.11.109>
- Wu, C., Chen, W., Zhang, H., Yu, H., Zhang, W., Jiang, N., & Liu, L. (2017). The hydration mechanism and performance of Modified magnesium oxysulfate cement by tartaric acid. *Construction and Building Materials*, 144, 516–524. <https://doi.org/10.1016/j.conbuildmat.2017.03.222>
- Zhang, C., Zuo, R., Zhang, J., & Wang, Y. (2015). Structure-dependent microwave dielectric properties and middle-temperature sintering of forsterite ( $Mg_{1-x}Ni_x$ )<sub>2</sub>SiO<sub>4</sub> ceramics. *Journal of the American Ceramic Society*, 98(3), 702–710. <https://doi.org/10.1111/jace.13347>
- Zhang, T., Vandeperre, L. J., & Cheeseman, C. R. (2014). Formation of magnesium silicate hydrate (M-S-H) cement pastes using sodium hexametaphosphate. *Cement and Concrete Research*, 65, 8–14. <https://doi.org/10.1016/j.cemconres.2014.07.001>